Chemical Science

ROYAL SOCIETY OF CHEMISTRY

EDGE ARTICLE

View Article Online
View Journal | View Issue

Cite this: *Chem. Sci.*, 2025, **16**, 11849

All publication charges for this article have been paid for by the Royal Society of Chemistry

Received 3rd April 2025
Accepted 27th May 2025

DOI: 10.1039/d5sc02515j

rsc.li/chemical-science

Identifying the superatomic $AuCu_{56}$ nanocluster through a ligand-exchange coupled metal-exchange induced transformation†

Saniya Gratious,[a] Bo Li,[b] Dipanjana Mondal,[c] Alok Kumar,[a] Dayona Aleyamma Varghese,[a] Jibin Thomas,[a] De-en Jiang,*[b] Vinayak Kamble[c] and Sukhendu Mandal*[a]

Quantum-sized metal nanoclusters can be viewed as superatoms that mimic the electron-shell closing behaviours of atoms, where these electronic shell configurations often govern their properties. Various superatomic nanoclusters with diverse structures and valence states have been identified over the past few years, but the 1S valence state of atomically precise Au nanoclusters has rarely been seen. Herein, we have achieved the synthesis of a $1S^1$ superatomic $[AuCu_{56}S_{12}(SAdm)_{20}(O_3SAdm)_{12}]$ nanocluster from the eight-electron $[Au_{23}(S\text{-}c\text{-}C_6H_{11})_{16}]^-$ nanocluster *via* a ligand-exchange coupled metal-exchange induced transformation. Detailed studies through mass spectrometry provided insights into the nanocluster formation, and theoretical studies revealed the superatomic nature of the nanocluster. Moreover, the as-synthesized nanocluster exhibited a broad optical absorption, leading to good photocurrent response under UV illumination. This work introduces a novel doping strategy that enables us to realize a rare superatomic valence state in an alloy cluster and to explore its unique light-induced properties.

Introduction

Atomically precise metal nanoclusters (NCs) have garnered substantial interest in recent years due to their extraordinary stability and intriguing physicochemical properties, with recent examples like an all-metal fullerene, $[K@Au_{12}Sb_{20}]^{5-}$ highlighting their expanding structural diversity.[1–5] Moreover, the ability of these NCs to mimic the properties of single atoms identifies them as "superatoms", where the superatomic core is stabilized by protecting ligands.[6–8] Analogous to the atomic theory, the "superatomic theory" also explains the stability and nature of these metal NCs, which are based on the guiding rules of compact geometry and electronic shell closing.[6] A well-studied example is the thiolate-protected $[Au_{25}(SR)_{18}]^-$ NC, which has an Au_{13} icosahedral core with three pairs of $Au_2(SR)_3$ staple motifs protecting the inner core. The exceptional stability of this $[Au_{25}(SR)_{18}]^-$ NC was explained by its closed-shell electronic configuration of $1S^21P^6$.[9] Several other superatomic NCs with various valence electron counts and diverse structures were also identified over the past few decades.[10–16] However, the guiding principles regarding the evolution of superatomic NCs as a function of their atomic arrangement have not yet been achieved. According to the superatom model, both the core composition and the surrounding ligands contribute towards the electronic stability of ligand protected NCs.[17–21] Hence, the manipulation of the photophysical properties of these superatomic NCs can be achieved by core or surface engineering.

Transformation chemistry has served as a versatile approach to manipulate the core and surface structures of atomically precise metal NCs and access novel NCs with diverse structures and intriguing properties.[22–25] Several methods of transformation have been developed over time, where the metal-exchange and ligand-exchange induced size/structure transformations have prevailed as superior techniques to tune the core and surface composition of metal NCs.[26–28] The metal-exchange induced size/structure transformation (MEIST) helps in understanding the doping effects on electronic structures and physicochemical properties of NCs,[22,25–27] whereas, the ligand-exchange induced size/structure transformation (LEIST) helps in understanding the effects of surface modulation.[27,29–32] To date, there are various examples of MEIST[33–45] and LEIST[29,46–50] reported on atomically precise NCs, however, the combined effect of both MEIST and LEIST on the structural growth patterns and corresponding property evolution of NCs is not yet explored. This gap in knowledge demands the need for

[a]*School of Chemistry, Indian Institute of Science Education and Research Thiruvananthapuram, Kerala 695551, India. E-mail: sukhendu@iisertvm.ac.in*

[b]*Department of Chemical and Biomolecular Engineering, Vanderbilt University, Nashville, TN 37235, USA. E-mail: de-en.jiang@vanderbilt.edu*

[c]*School of Physics, Indian Institute of Science Education and Research Thiruvananthapuram, Kerala 695551, India*

† Electronic supplementary information (ESI) available. CCDC 2426847. For ESI and crystallographic data in CIF or other electronic format see DOI: https://doi.org/10.1039/d5sc02515j

a thorough mechanistic study of these two techniques to advance the alloy NC library and understand their electronic and geometric structure evolution.

In this regard, we present a novel doping strategy that integrates both the ligand-exchange and metal-exchange methods on the eight-electron $[Au_{23}(S\text{-}c\text{-}C_6H_{11})_{16}]^-$ NC.[51] Investigations through time-dependent mass spectrometry underscored the occurrence of LEIST followed by MEIST on the precursor $[Au_{23}(S\text{-}c\text{-}C_6H_{11})_{16}]^-$ NC. Single-crystal X-ray diffraction (SCXRD) studies revealed the formation of an $[AuCu_{56}S_{12}(SAdm)_{20}(O_3SAdm)_{12}]$ (in short, $AuCu_{56}$) NC with an Au in the inner core. The theoretical calculations provided insights into the superatomic nature of the $AuCu_{56}$ NC with an electronic configuration of $1S^1$. This newly synthesized doped $AuCu_{56}$ NC exhibited good photocurrent response upon UV irradiation, with fast response and recovery times. This study not only enhances our understanding of the evolution of the electronic and geometric structure of superatomic bimetallic NCs but also paves the way for new applications and further exploration in the field of alloy NCs.

Results and discussion

Synthesis of the $AuCu_{56}$ nanocluster

The synthesis of $AuCu_{56}$ was achieved *via* the ligand-exchange induced size/structure transformation (LEIST) followed by metal-exchange of the $[Au_{23}(S\text{-}c\text{-}C_6H_{11})_{16}]^-$ (hereafter, Au_{23}) NC. The Au_{23} NC was synthesized and characterized by following the reported procedure.[51] The characteristic peak at 570 nm and the shoulder peak at 460 nm in the UV-vis absorption spectrum matched with the reported spectrum (Fig. S1a†). The matrix-assisted laser desorption ionization mass spectrometry (MALDI-MS) data showed a single peak at m/z = 6373.13 corresponding to the molecular-ion peak of the intact Au_{23} NC (Fig. S1b†). The transformation reaction was carried out by the addition of 1-adamantanethiol to the molecularly pure Au_{23} NC in DCM, followed by the addition of $Cu(CH_3CN)_4(BF_4)$ dissolved in CH_3CN (more information can be found in the ESI†). The transformation reaction was monitored through time-dependent UV-vis and MALDI-MS studies by taking aliquots from the reaction mixture at regular intervals. The UV-vis absorption spectra at the beginning of the reaction showed characteristic features of the Au_{23} NC, however in the presence of excess 1-adamantanethiol and Cu(I) salt, the absorption spectrum became almost featureless with weak absorption around 500 nm (Fig. S2†), which remained the same throughout the reaction. Time-dependent mass spectrometric studies of the aliquots were also carried out using MALDI-MS. At the beginning of the reaction (0 min), an intense peak at m/z = 6373.13 was observed, which corresponds to the intact $[Au_{23}(S\text{-}c\text{-}C_6H_{11})_{16}]^-$ NC (Fig. S3†). However, within 1 min of the addition of excess 1-adamantanethiol to the reaction mixture, peaks started appearing at m/z = 6488.30, 6175.82, and 5863.96, which correspond to $[Au_{23}(S\text{-}c\text{-}C_6H_{11})_{17}]$, $[Au_{22}(S\text{-}c\text{-}C_6H_{11})_{16}]$, and $[Au_{21}(S\text{-}c\text{-}C_6H_{11})_{15}]$, respectively. As time proceeds, these three peaks, along with a new peak at m/z = 6800.71 corresponding to $[Au_{24}(S\text{-}c\text{-}C_6H_{11})_{18}]$, indicate ligand-exchange with 1-adamantanethiol, which is evident from the formation of a new set of peaks with an equal spacing of 52 Da (difference between incoming adamantanethiol and existing cyclohexanethiol) (Table S1†). Subsequently, after 2 min, the Cu(I) salt was added to the reaction mixture, which entirely changed the mass spectral profile, and several new peaks were observed in the range of m/z = 4500–6500 (Fig. S4†). As the reaction advances, this broad range of peaks gradually narrowed to 5000–6000 m/z and further evolved into two sets of peaks ranging from m/z = 5000 to 6000 and from m/z = 6000 to 7000 by the end of 2 h. We carried out Electrospray Ionization Mass Spectrometry (ESI-MS) analysis of the aliquots at lower mass ranges (Fig. S5†), which showed peaks with a spacing of 133 Da corresponding to the difference between Au and Cu. This is attributed to the metal-exchange taking place during the transformation reaction. Hence, it can be inferred that the parent Au_{23} NC undergoes LEIST with adamanatanethiol, which in turn undergoes the metal-exchange with Cu (Scheme 1).

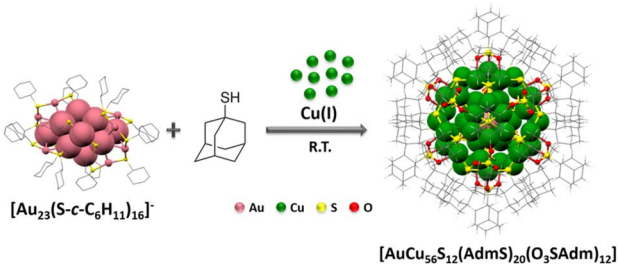

Scheme 1 Synthesis of the $AuCu_{56}$ NC from $[Au_{23}(S\text{-}c\text{-}C_6H_{11})_{16}]^-$ NC.

The reaction was allowed to proceed for 2 h at room temperature, and the reaction mixture was then washed with MeOH and extracted with DCM to remove unreacted starting materials. Unique six-legged "stellate" crystals were grown by layering the DCM solution of the as-obtained product with hexane (Fig. S6†) in three weeks (~10% yield, Cu-atom basis).

Crystal structure analysis

The star-shaped crystals were analyzed using SCXRD, which revealed the molecular formula of the NC to be $[AuCu_{56}S_{12}(SAdm)_{20}(O_3SAdm)_{12}]$ (hereafter $AuCu_{56}$) with a space group of *Pa*-3 (205) (Table S2†). The $AuCu_{56}$ NC structure possesses a C_3 symmetry and is composed of one Au atom, 56 Cu atoms, 12 S^{2-} ions, 20 adamantanethiolate ($C_{10}H_{15}S^-$) ligands, and 12 adamantane sulphonate ($C_{10}H_{15}SO_3^-$) ligands (Fig. 1a). The overall structure of the $AuCu_{56}$ can be visualized as an Au-centered double-shell copper framework, which is further protected by the thiolate ligands. This innermost Au atom (Fig. 1b) sourced from the Au_{23} parent NC, is surrounded by 14 Cu atoms arranged in the shape of a rhombic dodecahedron with 12 $[Cu_4]$ faces (Fig. 1c). This Cu_{14} inner core has an average Cu···Cu distance of 2.62 Å, which falls under the Cu···Cu van der Waals interaction range of 2.8 Å. The presence of a hollow $[Cu_{14}]$ core has been previously observed in a $[S\text{–}Cu_{50}]$ NC, with similar bonding patterns.[52] However, this work reports a high nuclearity $AuCu_{56}$ NC with a single Au-centered core, which is

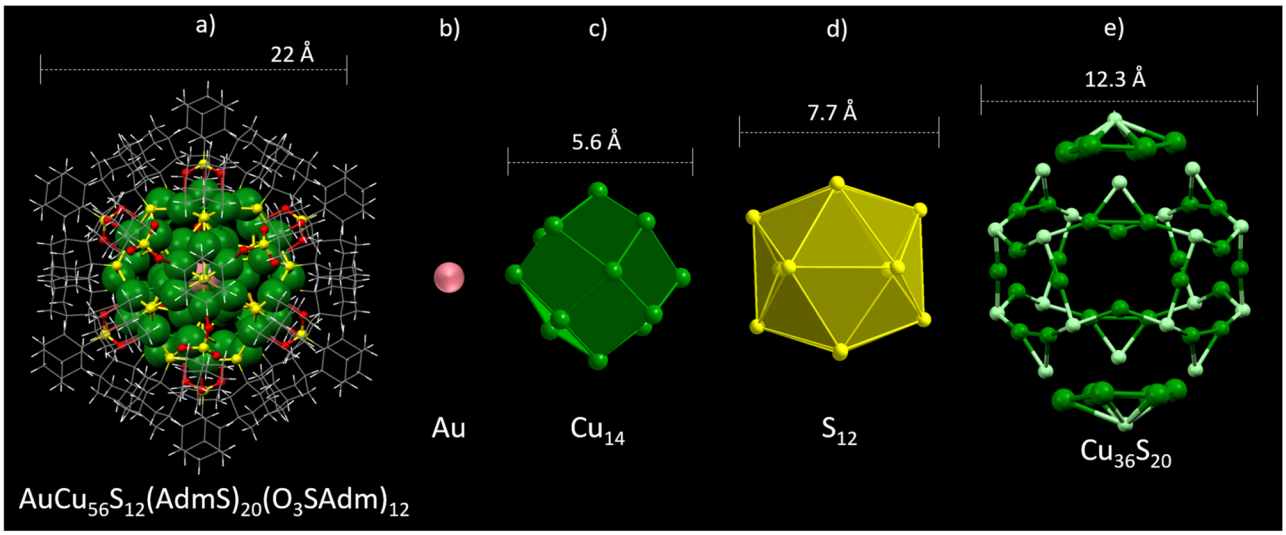

Fig. 1 Overview of the atomic structure of the $AuCu_{56}$ NC. (a) Total structure of the $AuCu_{56}$ NC. (b) The innermost Au atom present inside the (c) Cu_{14} cuboctahedron which is then connected to (d) a layer of 12 S^{2-} arranged in the shape of an icosahedron. (e) The atomic structure of the $Cu_{36}S_{20}$ outermost layer. Color code: pink, Au; green, Cu; yellow and light green, S; red, O; gray, C; white, H.

energetically favorable than the hollow ones.[53] In-depth structural analysis revealed that each of the $[Cu_4]$ face of the $[Cu_{14}]$ core is capped by one S^{2-} ion *via* μ^3-bridging with an average Cu···S distance of 2.27 Å (Fig. S7†). These 12 S^{2-} ions are arranged in the shape of an icosahedron with no S–S bonds between them (Fig. 1d), and therefore cannot be considered as a separate shell (average S–S distance of 4.07 Å). This $[Au@Cu_{14}S_{12}]$ shell is further protected by a $[Cu_{36}S_{20}]$ layer (Fig. 1e), where these S atoms are a part of the adamantanethiol ligands. This outermost layer can be divided into a $[Cu_{24}S_{18}]$ layer capped with two sets of $[Cu_6]$ units at the top and the bottom. The $[Cu_{24}S_{18}]$ layer can be viewed as an open-shell consisting of 3 pairs of $[Cu_5S_5]$ star-like motifs arranged around the waist of the $[Au@Cu_{14}S_{12}]$ shell (Fig. 2a). Each pair consists of two edge-sharing Cu_5S_5 stars with one motif facing upwards and the other downwards (Fig. 2b). Moreover, the inner S^{2-} layer is bound to three Cu atoms from each star motif *via* μ^3-bridging with an average Cu···S distance of 2.59 Å, showing an overall μ^6-bridging pattern. The same three Cu atoms of each star motif are further capped by one adamantane sulphonate ligand (Fig. 2c) formed *in situ* during the synthesis, yielding a total of 6 adamantane sulphonate ligands and 18 adamantanethiol ligands protecting the $[Cu_{24}S_{18}]$ layer (Fig. 2d). The $[Cu_{24}S_{18}]$ layer is capped by the hexagonal $[Cu_6]$ units (Fig. 2e) through its three alternate Cu atoms to the three apex S atoms of the $[Cu_{24}S_{18}]$ star motifs at the top and the bottom (Fig. 2f). These $[Cu_6]$ units are further protected by adamantanethiol ligands, giving rise to a closed $[Cu_{36}S_{20}(O_3S)_6]$ shell. The remaining six Cu atoms of the $AuCu_{56}$ NC connect this hexagonal $[Cu_6]$ unit with the $[Cu_{24}S_{18}]$ layer through adamantane sulphonate ligands with three at the top and three at the bottom in an η^2:η^1 fashion (Fig. 2g), forming the $[Cu_{42}S_{20}(O_3S)_6]$ (Fig. 2h). An interesting observation here is that the only Cu atoms that are bound to the inner S^{2-} layer bind to the adamantane sulphonate ligands in the outer layer. Every other Cu atom which only binds to the adamantanethiol ligands has no direct interaction with the inner S^{2-} layer. This reveals the driving force for the *in situ* oxidation of adamantanethiol ligands to give the adamantane sulphonate ligands.[54]

The $AuCu_{56}$ NC adopts a cubic geometry with each unit cell occupying twelve NCs at the edge centers and one at the body-center, making the effective number of molecules per unit cell 4 (Fig. S8†). The unit cell follows an AB-type stacking where the packing mode is directed by the intermolecular CH···HC non-bonding interactions of length ~2.28 Å (Fig. S9†). The previously reported $[S–Cu_{50}]$ also exhibits a similar geometry, however, its packing mode is directed by C–H···F hydrogen bonding, which extends the cubic NCs to an overall cubic superstructure,[52] whereas in this work, the intermolecular CH···HC interactions between the adamantane ligands act as the "sticky fingers" to extend the packing and give unique star-shaped crystals (Fig. S6†).

Characterizations

The optical microscopic images of the $AuCu_{56}$ crystals showed blackish star-like crystals of ~500 μm diameter with multiple branches resembling a snowflake (Fig. S6†). These crystals were characterized using Scanning Electron Microscopy (SEM) and Transmission Electron Microscopy (TEM) to understand their surface morphology and elemental composition. The SEM images showed a fern-like morphology for each of the branches with several terraces and steps on the surface (Fig. 3a). Several smaller branches were also observed to be originating from the center of the crystal. The TEM imaging of the crystals dispersed in MeOH showed a uniform distribution of spherical particles of size ~2.0 nm with little-to-no aggregation (Fig. S10a and b†). The elemental analysis confirmed the presence of Au, Cu, S, and O in appropriate amounts (Fig. S11†). X-ray photoelectron

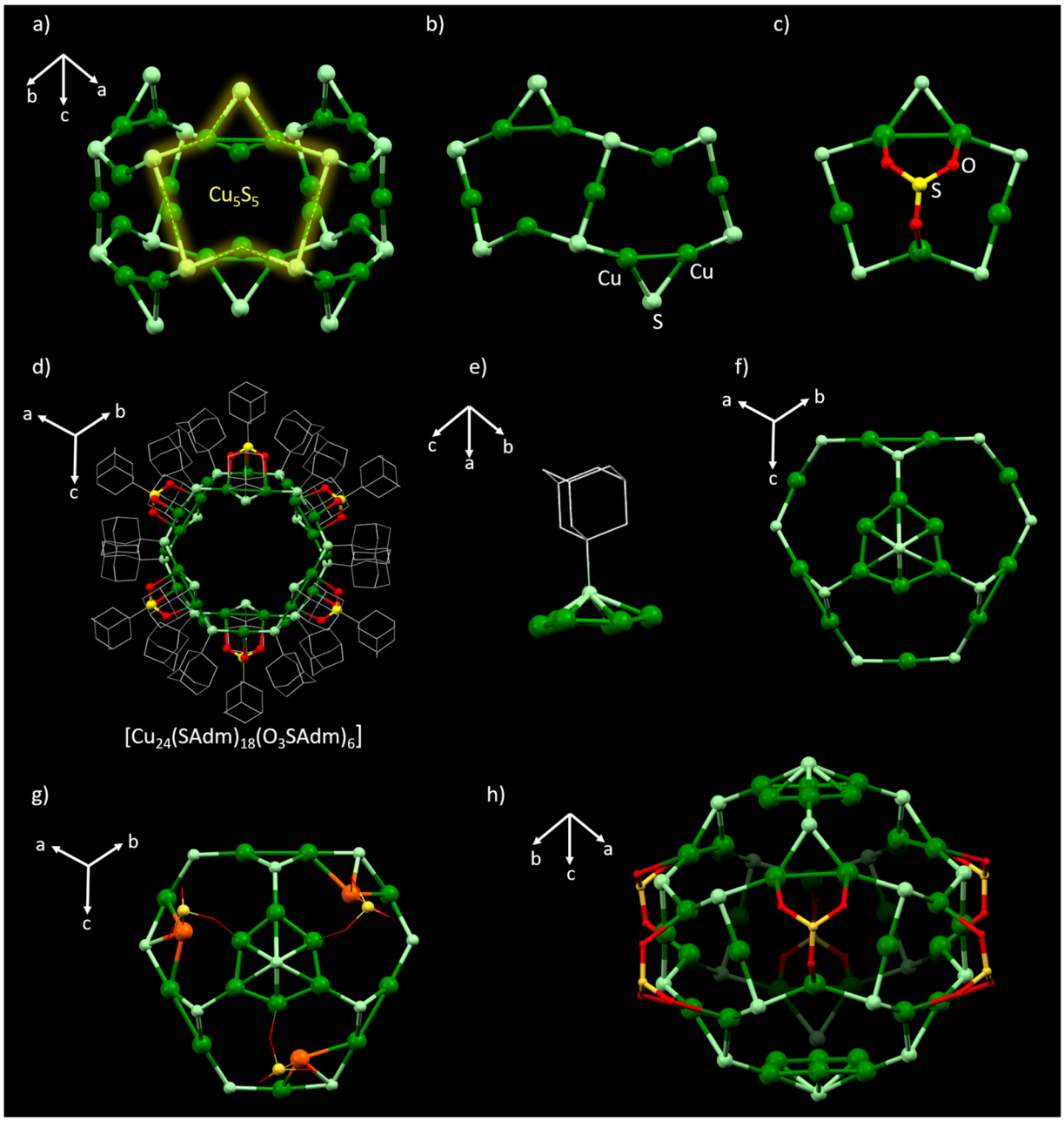

Fig. 2 Structural details of the $AuCu_{56}$ NC. (a) The outer $[Cu_{24}S_{18}]$ layer of the $AuCu_{56}$ NC. (b) The Cu_5S_5 star motif pair of the $[Cu_{24}S_{18}]$ layer, (c) binding of the adamantane sulphonate to the Cu_5S_5 star motif and (d) the $[Cu_{24}S_{18}]$ layer with the adamantane moieties. (e) The hexagonal $[Cu_6]$ unit capping the $[Cu_{24}S_{18}]$ layer and (f) top view of its binding mode. (g) Further connections between the $[Cu_{24}S_{18}]$ layer and the $[Cu_6]$ unit *via* three Cu atoms and finally the (h) overall $[Cu_{36}S_{26}(SO_3)_6]$ outermost layer excluding the adamantane moieties. Color code: pink, Au; green and orange, Cu; yellow and light green, S; red, O; gray, C. Hydrogen atoms are omitted for clarity.

spectroscopy (XPS) was done to confirm the composition of the $AuCu_{56}$ NC (Fig. 3b and c). The Au 4f XPS spectrum exhibited two broad peaks at 85.3 and 88.9 eV corresponding to the Au $4f_{7/2}$ and Au $4f_{5/2}$ spin–orbit components, respectively, which indicates an $Au^{\delta+}$ state of Au ($0 < \delta < +1$), in the inner core of the $AuCu_{56}$ NC (Fig. 3b).[55] The Cu XPS showed peaks at 930.5 eV and 950.3 eV corresponding to Cu $2p_{3/2}$ and Cu $2p_{1/2}$, respectively, with a significant split between the components, while a weak satellite peak was observed at ~943 eV, suggesting that the Cu atoms present in the NC are predominantly in +1 oxidation state (Fig. 3c).[56] The presence of two oxidation states for S was observed in the XPS, which is consistent with the structure modelled from SCXRD. The S 2p spectrum showed a prominent peak at 162.8 eV corresponding to the S^{2-} state and a weaker peak at 168.2 eV corresponding to the S^{5+} state from the adamantane sulphonate ligands (Fig. S12a†). Deconvolution of these peaks revealed the corresponding spin–orbit components with a spacing of ~1.1 eV. The survey spectrum (Fig. S12b†)

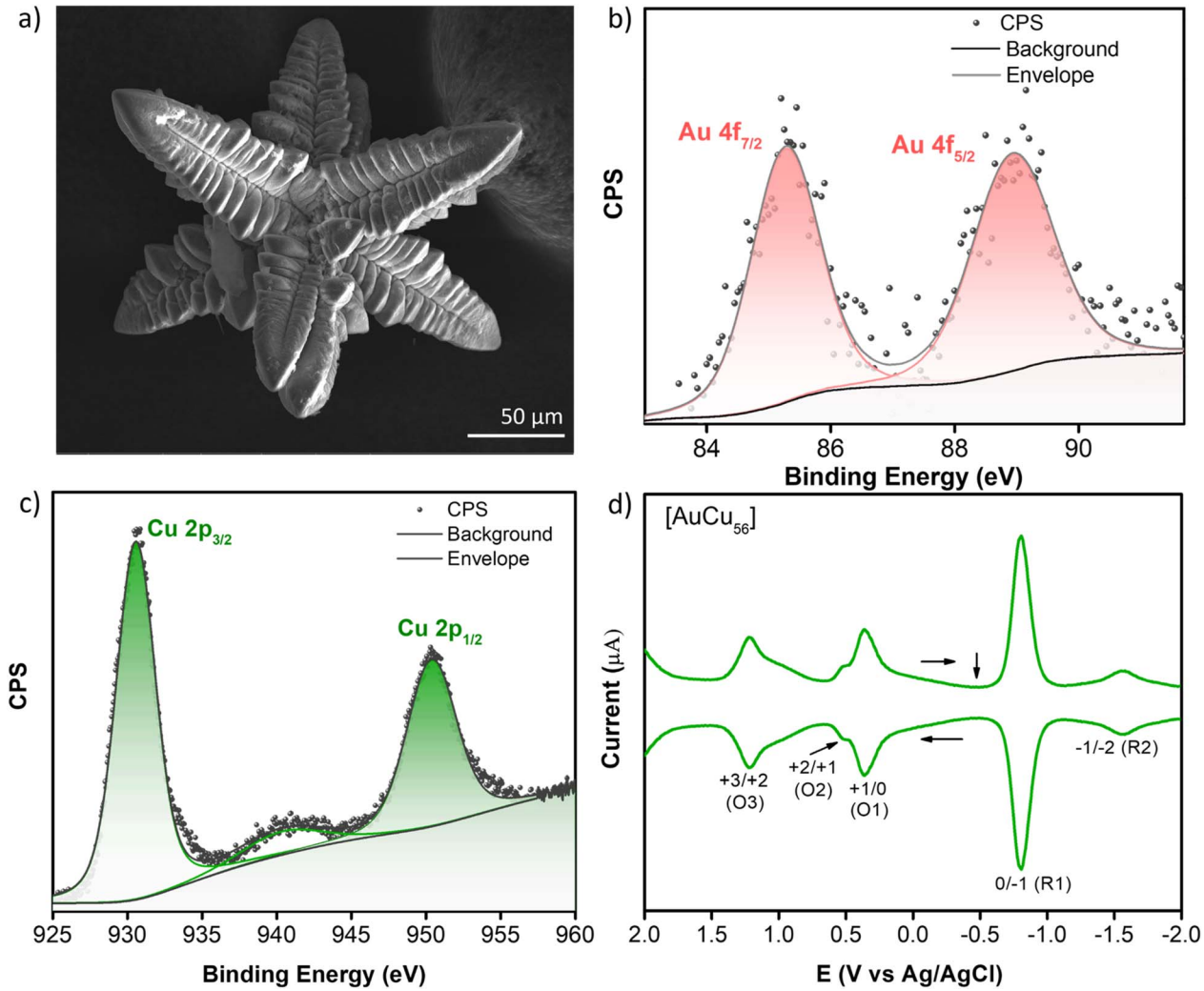

Fig. 3 (a) SEM image showing the star-shaped crystals with multiple branches. XPS spectra of the $AuCu_{56}$ NC showing the (b) Au 4f and (c) Cu 2p orbitals; (d) differential pulse voltammetry of $[AuCu_{56}S_{12}(AdmS)_{20}(O_3SAdm)_{12}]$ NC at a GC electrode (15 mm). DC potential ramp of 10 mV s^{-1} and a pulse amplitude of 50 mV.

shows the presence of all corresponding elements in the $AuCu_{56}$ NC.

To obtain a more comprehensive understanding of the electronic structures of the $AuCu_{56}$ NC, we carried out differential pulse voltammetry (DPV) measurements of the $AuCu_{56}$ NC (Fig. 3d). In Fig. S13,† the cyclic voltammograms and DPV are presented, where the blue vertical arrow highlights the first negative and positive redox peaks, and the horizontal arrow indicates the scanning direction. The clearly defined charging peaks are observed within the voltage range of −2 to +2 V. This phenomenon is attributed to the discrete charging of the NC at the electrode interface. This finding is indicative of the molecular-like electronic energy of the NC, which is influenced by the ultrasmall core dimension.[57] Fig. 3d illustrates the DPV of the NC measured across the same potential ranges. The peaks labelled O1, O2, and O3 correspond to the first, second, and third oxidation couples, respectively, while R1 and R2 represent the first and second reduction couples. An overview of these redox couples is provided in Table S4.† The electrochemical formal potential for the first one-electron oxidation of the NC is only slightly positive. A relatively negative potential is separated from the first oxidation potential by a significant energy gap of 1.17 V in MeCN (Fig. 3d). The energy gap comprises work terms linked to the charging of the NC $(AuCu_{56})^{+}$ and $(AuCu_{56})^{-}$, commonly termed charging or addition energy.[58] This estimation is derived from the difference between the formal potentials of $(AuCu_{56})^{+/0}$ and $(AuCu_{56})^{2+/1+}$, which is estimated as 0.13 V in MeCN as indicated in Table S4† (ox2–ox1). A corrected energy of 1.04 eV is derived from the difference, which serves as the electrochemical prediction for HOMO–LUMO gap energy.[59,60] The +2 and +3 oxidation states originate from the metallic core instead of the ligand, like the 3d-Cu shell manifold. These observations are in agreement with DFT calculations. The cyclic voltammogram (Fig. S14†) is reversible in nature in the wide range of redox window (*e.g.*, −2.0 to +2.0 V), which suggests even greater stability and redox flexibility and may serve as a plausible electron reservoir.

Electronic structure analysis

To further understand the electronic structure of the $AuCu_{56}$ NC, we performed density functional theory (DFT) calculations to first optimize its structure. Then we analyzed the frontier orbitals and spin density. Both HOMO and LUMO orbitals (Fig. 4a and b) were found to show clear superatomic features: the HOMO resembles an S orbital, while the LUMO a P orbital. This is fully consistent with the superatom complex theory[6] according to which the $AuCu_{56}$ NC will have only one free electron and a superatomic electron configuration of $1S^1$. While the distribution of HOMO or the 1S orbital concentrates on the central Au, it does extend to the Cu layers. This unpaired electron configuration of the $AuCu_{56}$ NC was further confirmed using electron paramagnetic resonance (EPR) spectroscopic measurements of the NC at 298 K, where an EPR signal with a *g*-tensor = 2.11 was observed (Fig. S15†).[61] The superatomic picture is further confirmed by the concentric bond analysis[62] of the $Au@Cu_{14}S_{12}@Cu_{36}$ core of the cluster (Fig. S16†), which shows a similar orbital concentration on the central Au but extends to the Cu_{14} layer. The atomic charge on the central gold atom was found to be +0.262 from the Mulliken population analysis, suggesting that it loses some fraction of its free electron to the Cu_{14} shell and beyond, consistent with the HOMO in Fig. 4a. The LUMO or 1P orbital is mainly located in the Cu layers. This means that there is a very intimate mixing of Au 6s and Cu 4s electrons, beyond a simplified picture of Au-centered Cu NC with the Cu atoms in the +1 state. The spin density distribution reinforces this idea: it is scattered around the center Au atom as well as around many Cu atoms (Fig. 4c).

Photocurrent response

The UV-vis absorption spectroscopy of the NC showed a broad absorption below 400 nm (Fig. 5a), which is commonly observed in high-nuclearity Cu NCs.[63–66] The onset of the absorption spectrum indicates a low band gap value. Owing to this UV range absorption and low band gap of the $AuCu_{56}$ NC, the photo-response of the sample was studied under UV illumination in a typical two-electrode system using the drop-casting method on a prefabricated Interdigitated Electrode (IDE) device over a Si/SiO_2 substrate with Cr/Au patterned electrodes (Fig. S17a†). Fig. 5b shows the *I–V* characteristics of the sample in the dark and under the illumination of a 360 nm laser (10 mW). Upon light irradiation, there is a clear change in the current compared to the dark condition, which confirms that the material generates a photocurrent, *i.e.*, electron–hole pair generation under the illumination of light. There is a clear offset in *I–V* characteristics under both dark and light conditions, which can be attributed to heterojunction formation in the sample. Upon applying a bias of 5 V through the device, ten on–off cycles with irradiation of 360 nm laser were observed (Fig. 5c). The blue shaded region shows the photoresponse observed under laser illumination. Each on–off cycle shows a constant change in the current, indicating its high stability over each cycle. A significant order of ~20 μA of photocurrent is generated for the 360 nm laser light with 10 mW of power. The device has a good response and recovery time of ~200 ms (Fig. S17b and c†), comparable to other NC-based materials.[67–71] Due to its broad absorption in the visible region, the photoresponse of the device was also tested with a white light source, which gave a photocurrent response of ~15 μA (Fig. S18†). This photocurrent response along with the DFT calculations directly link the $1S^1$ superatomic state to the photocurrent generation. The electronic structure analysis (Fig. 4a and b) shows that the HOMO is a superatomic 1S orbital and the LUMO is a 1P orbital. Importantly, the HOMO (1S) charge is concentrated at the central Au core while the LUMO (1P) lies on the Cu outer shell. Thus, photoexcitation moves the unpaired 1S electron from the core into a shell centered 1P level. This core shell shift naturally separates the photoelectron from its hole. Moreover, the spin-density distribution (Fig. 4c) shows that it is scattered on the Cu shell with little at Au, demonstrating that excitation produces an electron–hole pair with the electron on the periphery and the hole at the core. This arrangement is essential to yield efficient charge separation in analogous superatomic clusters.[67]

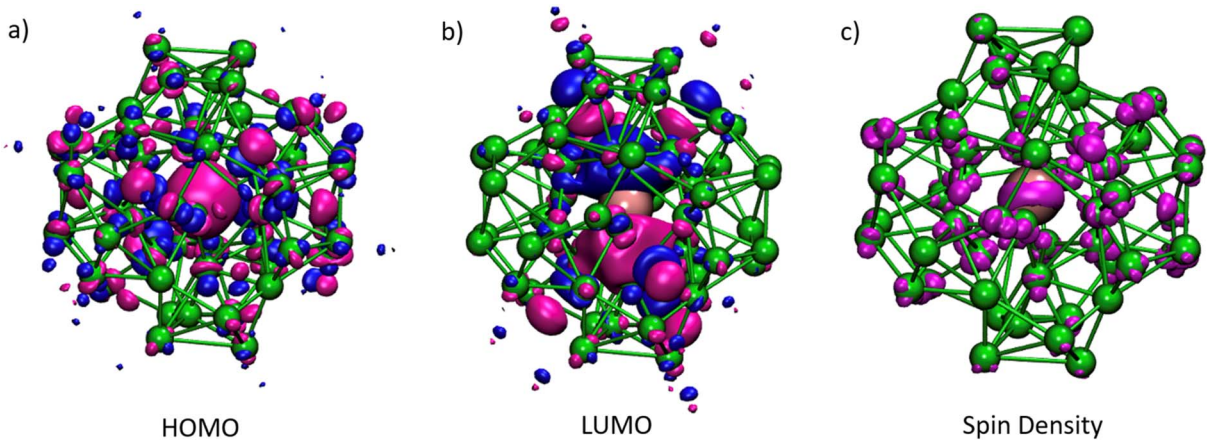

Fig. 4 (a) HOMO and (b) LUMO (magenta and blue isosurfaces) and (c) spin density (magenta isosurfaces) of the DFT-optimized $AuCu_{56}$ NC. Only the Au (pink) and Cu (green) atoms are shown; ligands are omitted for clarity.

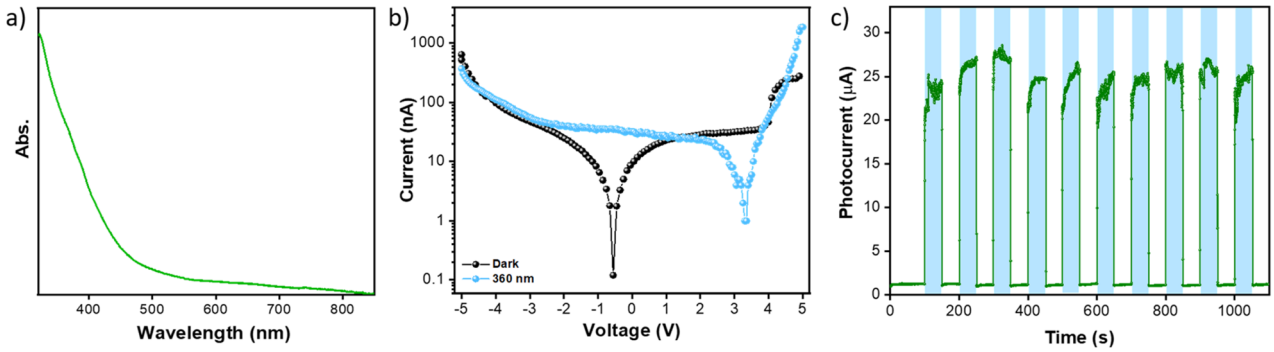

Fig. 5 (a) UV-vis absorption spectrum of the $AuCu_{56}$ crystals dispersed in DCM. (b) *I*–*V* characteristics of the device in the dark and 360 nm of laser illumination. (c) Photoresponse of the device under 360 nm laser irradiation, with the arrows indicating the response and recovery time of the device.

Thus, the $AuCu_{56}$ NC has a good generation and separation efficiency of the photoinduced electron–hole pairs as well as a good electron transport property, leading to a faster generation or decay of the photocurrent under light illumination or dark conditions, respectively.

Conclusions

In summary, a superatomic $[AuCu_{56}S_{12}(SAdm)_{20}(O_3SAdm)_{12}]$ NC was synthesized from an eight-electron $[Au_{23}(S\text{-}c\text{-}C_6H_{11})_{16}]^-$ NC through a ligand exchange coupled metal-exchange induced transformation. The time-dependent mass spectrometric studies showed that the simultaneous occurrence of LEIST and MEIST led to the formation of $AuCu_{56}$ NC. This NC can be viewed as a unique Au-centered double-shell copper framework protected by thiolate ligands. The electronic structure calculations revealed an electronic configuration of $1S^1$ for the superatomic $AuCu_{56}$. The electrochemical studies and the theoretical calculations revealed the low band gap of the material, validating the good photoresponse of the material upon UV irradiation with a good response and recovery time. This unique synthetic strategy allowed us to understand the evolution of the superatomic bimetallic NC and promotes the rational design of metal NCs for future applications.

Data availability

ESI† contains experimental details, structural details, MALDI and ESI-MS, TEM, XPS, and CV data and measurement details, theoretical calculation details, crystal structure parameters, selected bond lengths, and photo-current data.

Author contributions

S. G. designed and performed the synthesis, characterization, and data interpretation with the assistance from J. T. and D. V. B. L. and D. J. performed the theoretical calculations. A. K. performed the electrochemical measurements. The photocurrent measurements were conducted by D. M. and V. K. S. M. conceived and supervised the project, and was involved in data analysis. All authors were involved in the discussion of results and manuscript writing.

Conflicts of interest

The authors declare no competing interest.

Acknowledgements

Funding for the project was obtained from the Science and Engineering Research Board (SERB) through the grants CRG/2022/000984. AK thanks the Science and Engineering Research Board (SERB), Government of India, for a National Post-Doctoral Fellowship (PDF/2023/002916). DFT computation (BL and DJ) was supported by the U.S. Department of Energy, Office of Science, Office of Basic Energy Sciences, Chemical Sciences, Geosciences, and Bio-sciences Division, Catalysis Science Program.

References

1 R. Jin, C. Zeng, M. Zhou and Y. Chen, *Chem. Rev.*, 2016, **116**, 10346–10413.
2 Y. Du, H. Sheng, D. Astruc and M. Zhu, *Chem. Rev.*, 2020, **120**, 526–622.
3 I. Chakraborty and T. Pradeep, *Chem. Rev.*, 2017, **117**, 8208–8271.
4 R. Jin, G. Li, S. Sharma, Y. Li and X. Du, *Chem. Rev.*, 2021, **121**, 567–648.
5 Y.-H. Xu, W.-J. Tian, A. Muñoz-Castro, G. Frenking and Z.-M. Sun, *Science*, 2023, **382**, 840–843.
6 M. Walter, J. Akola, O. Lopez-Acevedo, P. D. Jadzinsky, G. Calero, C. J. Ackerson, R. L. Whetten, H. Grönbeck and H. Häkkinen, *Proc. Natl. Acad. Sci. U. S. A.*, 2008, **105**, 9157–9162.
7 H. Häkkinen, *Chem. Soc. Rev.*, 2008, **37**, 1847.
8 M. Zhu, C. M. Aikens, F. J. Hollander, G. C. Schatz and R. Jin, *J. Am. Chem. Soc.*, 2008, **130**, 5883–5885.
9 M. A. Tofanelli and C. J. Ackerson, *J. Am. Chem. Soc.*, 2012, **134**, 16937–16940.

10 T. Omoda, S. Takano and T. Tsukuda, *Small*, 2021, **17**, 2001439–2001457.
11 C. P. Joshi, M. S. Bootharaju, M. J. Alhilaly and O. M. Bakr, *J. Am. Chem. Soc.*, 2015, **137**, 11578–11581.
12 P. D. Jadzinsky, G. Calero, C. J. Ackerson, D. A. Bushnell and R. D. Kornberg, *Science*, 2007, **318**, 430–433.
13 H. Häkkinen, M. Walter and H. Grönbeck, *J. Phys. Chem. B*, 2006, **110**, 9927–9931.
14 K. Nunokawa, S. Onaka, M. Ito, M. Horibe, T. Yonezawa, H. Nishihara, T. Ozeki, H. Chiba, S. Watase and M. Nakamoto, *J. Organomet. Chem.*, 2006, **691**, 638–642.
15 C. E. Briant, B. R. C. Theobald, J. W. White, L. K. Bell, D. M. P. Mingos and A. J. Welch, *J. Chem. Soc. Chem. Commun.*, 1981, 201–202.
16 L. C. McKenzie, T. O. Zaikova and J. E. Hutchison, *J. Am. Chem. Soc.*, 2014, **136**, 13426–13435.
17 S. Takano and T. Tsukuda, *J. Am. Chem. Soc.*, 2021, **143**, 1683–1698.
18 H. Yi, S. M. Han, S. Song, M. Kim, E. Sim and D. Lee, *Angew. Chem., Int. Ed.*, 2021, **60**, 22293–22300.
19 A. Tlahuice-Flores and A. Muñoz-Castro, *Int. J. Quantum Chem.*, 2019, **119**, e25756–e25768.
20 E. Ito, S. Takano, T. Nakamura and T. Tsukuda, *Angew. Chem., Int. Ed.*, 2021, **60**, 645–649.
21 R. Saito, K. Isozaki, Y. Mizuhata and M. Nakamura, *J. Am. Chem. Soc.*, 2024, **146**, 20930–20936.
22 C. Zeng, Y. Chen, A. Das and R. Jin, *J. Phys. Chem. Lett.*, 2015, **6**, 2976–2986.
23 K. R. Krishnadas, A. Baksi, A. Ghosh, G. Natarajan and T. Pradeep, *Nat. Commun.*, 2016, **7**, 13447.
24 S. Gratious, S. Mukherjee and S. Mandal, *J. Phys. Chem. Lett.*, 2022, **13**, 9014–9027.
25 S. Gratious, E. N. Nahan, R. Jin and S. Mandal, *Acc. Mater. Res.*, 2024, **5**, 1291–1302.
26 X. Kang, Y. Li, M. Zhu and R. Jin, *Chem. Soc. Rev.*, 2020, **49**, 6443–6514.
27 X. Kang and M. Zhu, *Chem. Mater.*, 2019, **31**, 9939–9969.
28 Y. Kim, S. Ji and J.-M. Nam, *Acc. Chem. Res.*, 2023, **56**, 2139–2215.
29 C. Zeng, C. Liu, Y. Pei and R. Jin, *ACS Nano*, 2013, **7**, 6138–6145.
30 W. Suzuki, R. Takahata, Y. Chiga, S. Kikkawa, S. Yamazoe, Y. Mizuhata, N. Tokitoh and T. Teranishi, *J. Am. Chem. Soc.*, 2022, **144**, 12310–12320.
31 X. Meng, Q. Xu, S. Wang and M. Zhu, *Nanoscale*, 2012, **4**, 4161.
32 S. Yang, J. Chai, Y. Song, J. Fan, T. Chen, S. Wang, H. Yu, X. Li and M. Zhu, *J. Am. Chem. Soc.*, 2017, **139**, 5668–5671.
33 Q. Li, K. J. Lambright, M. G. Taylor, K. Kirschbaum, T. Y. Luo, J. Zhao, G. Mpourmpakis, S. Mokashi-Punekar, N. L. Rosi and R. Jin, *J. Am. Chem. Soc.*, 2017, **139**, 17779–17782.
34 Y. Negishi, T. Iwai and M. Ide, *Chem. Commun.*, 2010, **46**, 4713.
35 Q. Li, T.-Y. Luo, M. G. Taylor, S. Wang, X. Zhu, Y. Song, G. Mpourmpakis, N. L. Rosi and R. Jin, *Sci. Adv.*, 2017, **3**, e1603193–e1603200.
36 S. Wang, Y. Song, S. Jin, X. Liu, J. Zhang, Y. Pei, X. Meng, M. Chen, P. Li and M. Zhu, *J. Am. Chem. Soc.*, 2015, **137**, 4018–4021.
37 M. S. Bootharaju, L. Sinatra and O. M. Bakr, *Nanoscale*, 2016, **8**, 17333–17339.
38 M. Zhu, P. Wang, N. Yan, X. Chai, L. He, Y. Zhao, N. Xia, C. Yao, J. Li, H. Deng, Y. Zhu, Y. Pei and Z. Wu, *Angew. Chem., Int. Ed.*, 2018, **57**, 4500–4504.
39 N. Xia and Z. Wu, *J. Mater. Chem. C*, 2016, **4**, 4125–4128.
40 C. Yao, J. Chen, M. B. Li, L. Liu, J. Yang and Z. Wu, *Nano Lett.*, 2015, **15**, 1281–1287.
41 Z. Wu, *Angew. Chem., Int. Ed.*, 2012, **51**, 2934–2938.
42 M. S. Bootharaju, C. P. Joshi, M. R. Parida, O. F. Mohammed and O. M. Bakr, *Angew. Chem., Int. Ed.*, 2016, **55**, 922–926.
43 K. R. Krishnadas, A. Ghosh, A. Baksi, I. Chakraborty, G. Natarajan and T. Pradeep, *J. Am. Chem. Soc.*, 2016, **138**, 140–148.
44 K. R. Krishnadas, A. Baksi, A. Ghosh, G. Natarajan and T. Pradeep, *ACS Nano*, 2017, **11**, 6015–6023.
45 S. Bhat, A. Baksi, S. K. Mudedla, G. Natarajan, V. Subramanian and T. Pradeep, *J. Phys. Chem. Lett.*, 2017, **8**, 2787–2793.
46 M. M. Maman, N. N. E. K, G. Suresh, A. Das, A. S. Nair, B. Pathak and S. Mandal, *Nanoscale*, 2023, **15**, 13102–13109.
47 S. Gratious, A. Afreen, E. Mahal, J. Thomas, S. Saha, A. S. Nair, K. V. Adarsh, B. Pathak and S. Mandal, *Chem. Sci.*, 2024, **15**, 9823–9829.
48 N. N. Eyyakkandy, A. Afreen, G. Vilangappurath, S. Gratious, K. V. Adarsh and S. Mandal, *J. Phys. Chem. C*, 2024, **128**, 18828–18835.
49 X. Kang, M. Ren, M. Zhu and K. Zhang, *Chem. Mater.*, 2020, **32**, 6736–6743.
50 Y. Niihori, Y. Kikuchi, A. Kato, M. Matsuzaki and Y. Negishi, *ACS Nano*, 2015, **9**, 9347–9356.
51 A. Das, T. Li, K. Nobusada, C. Zeng, N. L. Rosi and R. Jin, *J. Am. Chem. Soc.*, 2013, **135**, 18264–18267.
52 C. Xu, Y. Jin, H. Fang, H. Zheng, J. C. Carozza, Y. Pan, P.-J. Wei, Z. Zhang, Z. Wei, Z. Zhou and H. Han, *J. Am. Chem. Soc.*, 2023, **145**, 25673–25685.
53 X. Kang, X. Wei, X. Liu, S. Wang, T. Yao, S. Wang and M. Zhu, *Nat. Commun.*, 2021, **12**, 6186.
54 L.-J. Liu, J.-W. Zhang, M. Asad, Z.-Y. Wang, S.-Q. Zang and T. C. W. Mak, *Chem. Commun.*, 2021, **57**, 5586–5589.
55 M. P. Casaletto, A. Longo, A. Martorana, A. Prestianni and A. M. Venezia, *Surf. Interface Anal.*, 2006, **38**, 215–218.
56 A. K. Das, S. Biswas, A. Pal, S. S. Manna, A. Sardar, P. K. Mondal, B. Sahoo, B. Pathak and S. Mandal, *Nanoscale*, 2024, **16**, 3583–3590.
57 Y. Yang and S. Chen, *Nano Lett.*, 2003, **3**, 75–79.
58 C. Creutz, B. S. Brunschwig and N. Sutin, in *Comprehensive Coordination Chemistry II*, 2003, vol. 7, pp. 731–777.
59 Y. Negishi, K. Munakata, W. Ohgake and K. Nobusada, *J. Phys. Chem. Lett.*, 2012, **3**, 2209–2214.
60 D. Lee, R. L. Donkers, G. Wang, A. S. Harper and R. W. Murray, *J. Am. Chem. Soc.*, 2004, **126**, 6193–6199.
61 M. Agrachev, M. Ruzzi, A. Venzo and F. Maran, *Acc. Chem. Res.*, 2019, **52**, 44–52.

62 A. Muñoz-Castro, *ChemPhysChem*, 2025, **26**, e202400892.
63 A. Baghdasaryan and T. Bürgi, *Nanoscale*, 2021, **13**, 6283–6340.
64 B.-L. Han, Z. Liu, L. Feng, Z. Wang, R. K. Gupta, C. M. Aikens, C.-H. Tung and D. Sun, *J. Am. Chem. Soc.*, 2020, **142**, 5834–5841.
65 A. Baghdasaryan, C. Besnard, L. M. Lawson Daku, T. Delgado and T. Burgi, *Inorg. Chem.*, 2020, **59**, 2200–2208.
66 R.-W. Huang, J. Yin, C. Dong, A. Ghosh, M. J. Alhilaly, X. Dong, M. N. Hedhili, E. Abou-Hamad, B. Alamer, S. Nematulloev, Y. Han, O. F. Mohammed and O. M. Bakr, *J. Am. Chem. Soc.*, 2020, **142**, 8696–8705.
67 S. Biswas, A. K. Das, A. C. Reber, S. Biswas, S. Bhandary, V. B. Kamble, S. N. Khanna and S. Mandal, *Nano Lett.*, 2022, **22**, 3721–3727.
68 Z. Wang, L. Li, L. Feng, Z. Gao, C. Tung, L. Zheng and D. Sun, *Angew. Chem., Int. Ed.*, 2022, **61**, 823–832.
69 Z. Wang, Y.-J. Zhu, B.-L. Han, Y.-Z. Li, C.-H. Tung and D. Sun, *Nat. Commun.*, 2023, **14**, 5295.
70 W.-X. Xie, C.-H. Xue, M. Liu, K. Zhou, H.-H. Gu, J.-Y. Ji, B.-K. Chen, N. Liu and Y.-F. Bi, *Dalton Trans.*, 2023, **52**, 13405–13412.
71 H. Zhao, C. Zhang, B. Han, Z. Wang, Y. Liu, Q. Xue, C.-H. Tung and D. Sun, *Nat. Synth.*, 2024, **3**, 517–526.